Energy Advances

ROYAL SOCIETY OF CHEMISTRY

PAPER

View Article Online
View Journal | View Issue

Cite this: *Energy Adv.*, 2024, 3, 894

Stress-induced stabilization of the photoactive $FAPbI_3$ phase under ambient conditions without using an additive approach†

Shivam Porwal, [a] Nitin Kumar Bansal, [b] Subrata Ghosh [a] and Trilok Singh*[ab]

Formamidinium lead iodide ($FAPbI_3$) as the absorber material has garnered significant interest due to its suitable bandgap for perovskite solar cell applications. Herein, a novel fabrication process is developed to stabilize the photoactive alpha phase of $FAPbI_3$. This approach involves the formation of an intermediate phase and the introduction of strain within the perovskite film. The strain in the perovskite film is generated because of the interfacial lattice mismatch between the perovskite and SnO_2 (electron transport layer) and the temperature difference between the substrate and the perovskite precursor solution. The microstructural stress analysis using X-ray diffraction (XRD) and photoluminescence spectroscopy (PL) analysis confirm the strain within the film. The fabricated perovskite film remained stable and without transforming into δ-$FAPbI_3$ even after being exposed to air for three months. The fabricated solar cells demonstrated a power conversion efficiency (PCE) of 20.46% with excellent reproducibility. Moreover, the non-encapsulated device retained normalized PCE above 85% when stored under relative humidity levels below 40% for 1200 hours. Therefore, this study provides a method of stabilizing alpha-phase $FAPbI_3$-based perovskite solar cells without using additive approaches.

Received 9th February 2024,
Accepted 13th March 2024

DOI: 10.1039/d4ya00092g

rsc.li/energy-advances

1. Introduction

Organic metal halide perovskites (OHPs) have shown potential for optoelectronic applications, particularly in the realm of solar cells. This is attributed to their exceptional characteristics, which encompass a suitable direct bandgap, relatively high optical absorption, defect tolerance, and efficacious properties for transporting charge carriers.[1–11] The power conversion efficiency (PCE) of perovskite solar cells (PSCs) has significantly increased, with PCE for single junction cells approaching 26.08% due to advancements in material processing and device optimization.[12] These solar cells exhibit a high PCE because of a suitable direct bandgap (~1.48 eV) that enables efficient photon absorption. Furthermore, PSCs utilizing $FAPbI_3$ displayed a notable decline in non-radiative recombination losses, resulting in high short-circuit currents and enhanced photovoltaic PCE.[13,14] Moreover, this material exhibits higher thermal and photostability compared to other OHPs due to the presence of a FA cation ($NH_2CH{=}NH_2^+$), which necessitates significant activation energy for thermal degradation. However, the three-dimensional α-$FAPbI_3$ is metastable at room temperature (R.T.) and rapidly converted into the one dimensional δ-$FAPbI_3$ phase because of the larger cationic size of FA (tolerance factor ~1), which drives phase transition from the photoactive cubic phase (α-$FAPbI_3$) to the photoinactive hexagonal phase (δ-$FAPbI_3$).[15–18] The occurrence of polymorphic phase transformation in α-$FAPbI_3$ (cubic phase) is primarily contingent upon the orientation of the FA^+ cation at varying temperatures. On the other hand, δ-$FAPbI_3$ (hexagonal phase) has a lower formation enthalpy, which renders it stable at R.T. As the temperature is raised from R.T. to 150 °C, the transformation from the hexagonal to the cubic phase is driven by entropy resulting from stress generated by the varying orientations of the larger A-site cation. During this phase transition, the FA^+ cation adopts different orientations, leading to dissimilar entropy values. This represents a significant and critical challenge for stabilizing the pure α-$FAPbI_3$ phase at room temperature. Additionally, the fabrication of $FAPbI_3$ films and the crystallization of the α-$FAPbI_3$ phase encounter various obstacles due to the large ionic radius of the FA^+ molecule at the A site. To address this problem, researchers have introduced a very small amount of MA^+, Rb^+ and Cs^+ cations for partial replacement of the A-site cation. Along with this, mixed halides also being used at the X-site into the perovskite structure. This approach helps to thermodynamically stabilize the perovskite phase.[19–21]

[a] *School of Energy Science and Engineering, Indian Institute of Technology Kharagpur, Kharagpur, 721302, India. E-mail: triloksingh@dese.iitd.ac.in*
[b] *Semiconductor Thin Film and Emerging Photovoltaic Laboratory, Department of Energy Science and Engineering, Indian Institute of Technology Delhi, Hauz Khas, New Delhi 110016, India*

† Electronic supplementary information (ESI) available. See DOI: https://doi.org/10.1039/d4ya00092g

Unfortunately, mixed perovskites are susceptible to long-term phase instability due to an increase in the enthalpy of the system. Furthermore, at elevated temperatures (~150 °C), the replaced A-site cations (MA^+, Rb^+ and Cs^+) and halides may begin to migrate due to their low diffusion energy.[22,23] Therefore, it is essential to achieve stabilization of the additive-free pure α-$FAPbI_3$ for the fabrication of thermally stable and efficient PSCs suitable for commercial applications.

In the present study, we have introduced a novel fabrication approach for stabilizing the α-$FAPbI_3$ phase. This method entails the generation of an intermediate phase and the introduction of strain at the interface between the electron transport layer (ETL) and the perovskite film. The strain is produced by the lattice mismatch between the perovskite and SnO_2 (ETL), as well as due to the temperature difference between the substrate and the perovskite precursor solution. The formation of the intermediate phase is substantiated by the presence of an X-ray diffraction (XRD) peak at 8.2°, while the estimation of interfacial stress is accomplished through microstructural stress analysis. When examining the film grown on a SnO_2 coated glass substrate, a significant tensile stress of 140.87 MPa is observed; in contrast, the film on a glass substrate exhibits a notably lower tensile stress of 2.96 MPa. This disparity is further supported by the blue shift evident in both XRD and photoluminescence spectroscopy (PL), which supports the increased tensile stress in the film grown over the SnO_2 coated glass substrate. Remarkably, even after three-month exposure to ambient air, there is no evidence of δ-$FAPbI_3$ in the film produced using the proposed method on the SnO_2 substrate. Notably, the best performing solar cell showed an impressive PCE of 20.46%, and the unencapsulated device retained normalized PCE above 85% under relative humidity levels lower than 40%, up to 1200 hours. We believe this to be the first thorough study on the stabilization of additive-free $FAPbI_3$-based PSCs under air ambient conditions.

2. Results and discussion

2.1. Stabilization of α-$FAPbI_3$

(a) Formation of the Intermediate phase. The quality of α-$FAPbI_3$ films is largely influenced by a slow crystallization rate which facilitates the formation of an intermediate phase. This intermediate phase impedes the transformation of the cubic photoactive black α-$FAPbI_3$ phase into the photoinactive yellow hexagonal δ-$FAPbI_3$ phase, thereby promoting the high-quality α-$FAPbI_3$ film. During annealing, the high evaporation temperature (189 °C) of the solvent dimethyl sulfoxide (DMSO) and its strong coordination with lead ions contribute to the slow removal of DMSO. This slow removal of DMSO enhances the overall crystallinity of the perovskite film. It is noteworthy that the optimal quantity of DMSO in the solution of formamidinium iodide (FAI), lead iodide (PbI_2), and dimethylformamide (DMF), coupled with the introduction of an antisolvent prior to the end of the spin coating procedure, leads to the formation of an FAI-PbI_2-DMSO intermediate phase immediately upon completion of the spin coating process. In this context, PbI_2 functions as a Lewis acid, while both FAI and DMSO act as Lewis bases. The interaction between these Lewis acid and base pairs results in the formation of a Lewis acid–base adduct. The formation of the intermediate phase can be predominantly attributed to the presence of this adduct, which is additionally

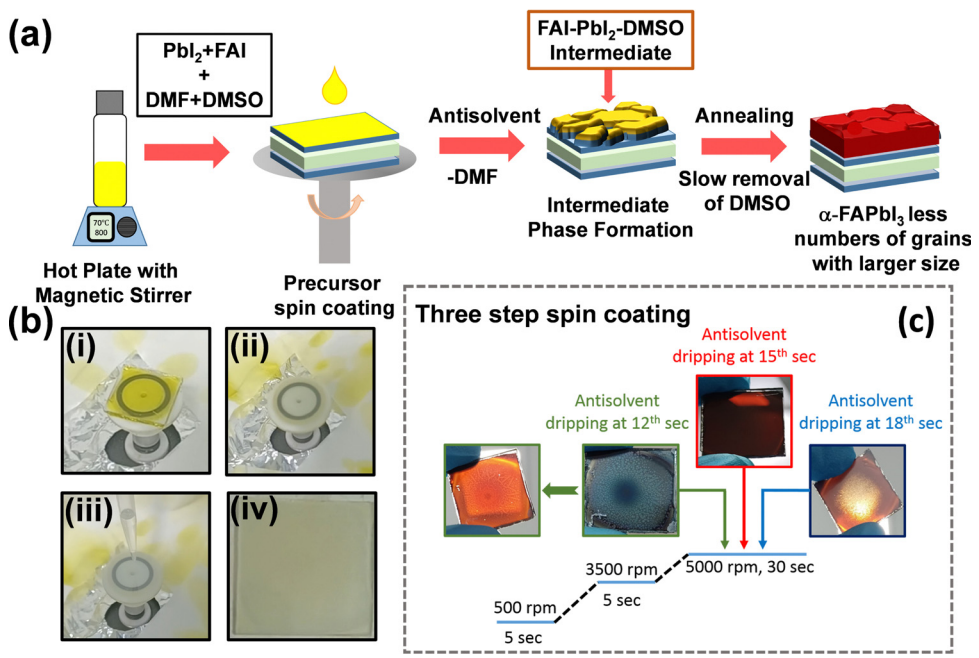

Fig. 1 (a) Deposition of the $FAPbI_3$ precursor solution *via* a spin coater, (b) (i) dropping of solution on the substrate, (ii) spin coating of solution, (iii) dripping of anti-solvent, and (iv) FAI-PbI_2-DMSO intermediate phase, and (c) schematic of the spin coating process and quality of the film formed after antisolvent dripping at various time intervals.

facilitated by the introduction of an antisolvent during the spin-coating process.[24–26] In this study, we initially optimized the processing parameters for the fabrication of perovskite films on both glass and SnO_2-coated FTO substrates, as outlined in Tables S1 and S2 (ESI†). Thus, the $FAPbI_3$ perovskite film was obtained by mixing FAI (0.7 M) and PbI_2 (0.7 M) in 1 mL of DMF and DMSO mixed solvent (3 : 1). Then the solution was stirred at 70 °C for 60 minutes, and spin coated on substrates using a three step spin coating process. During the 15th second of the final stage (3rd step) of the spin-coating process, 250 μL of antisolvent (toluene) was introduced. This step aids in the formation of the intermediate phase, as depicted in Fig. 1a and b. It is also noticed that antisolvent dripping at time other than the 15th second of the final stage (3rd step) of the spin-coating process does not provide a good quality film after annealing because of excess formation of nuclei or early crystallization of the α-$FAPbI_3$ phase, as shown in Fig. 1c. The formed intermediate phase of FAI-PbI_2-DMSO highly depends on the way the antisolvent is applied.

The films formed after antisolvent dripping (without annealing) were characterized by XRD and SEM. An intense peak (2 theta = 8.2°) in the X-ray diffraction pattern was recorded (Fig. 2), which indicated the formation of the FAI-PbI_2-DMSO intermediate phase.[26,27] To enhance the crystallization and formation of the photoactive α-$FAPbI_3$ phase, the substrates were subjected to bottom-up heating. The slow removal of DMSO from the FAI-PbI_2-DMSO intermediate phase results in a high degree of crystallinity in the α-$FAPbI_3$ film. The XRD results indicated that the formed intermediate phase remained stable at temperatures of up to 150 °C. After annealing for 30 minutes at 150 °C, the intermediate phase completely transformed into the α-$FAPbI_3$ phase.

This phase conversion tends to minimize the overall free energy of the system, leading to a change in the grain size.[28]

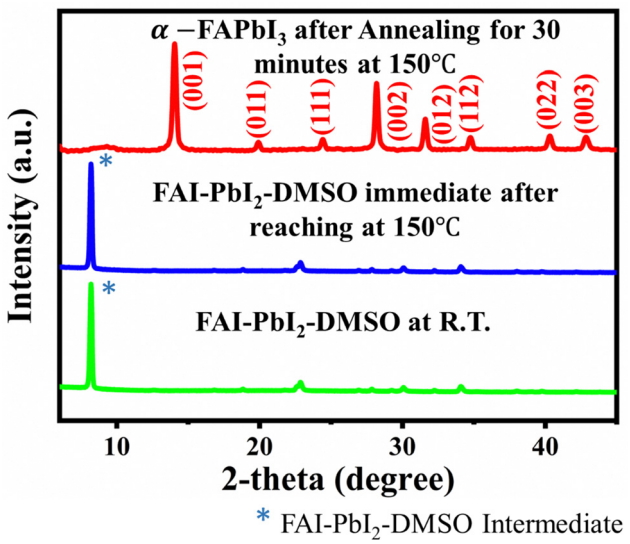

Fig. 2 Formation of the FAI-PbI_2-DMSO intermediate phase at room temperature (R.T.), the intermediate phase which remained stable up to 150 °C, and complete conversion of the intermediate phase to the α-$FAPbI_3$ phase after annealing.

The change in grain size during crystallization can be clearly visualized through SEM images. The SEM images (top-view) of samples without annealing, during annealing (reaching 150 °C), and after annealing at 150 °C for 30 minutes have been taken at various magnifications as shown in Fig. 3a–f. On observing Fig. 3a and b at different magnifications, it becomes evident that the spin coating process resulted in the formation of rod-shaped larger grains of the intermediate phase, as previously reported. These grains had dimensions of up to a few micrometres.[27] To facilitate the transition from the intermediate phase to the α-$FAPbI_3$ phase, the substrates were subjected to annealing on a hot plate at 150 °C for a duration of 30 minutes. In this process after reaching 150 °C, the SEM images (Fig. 3c and d) are showing the transformation of the intermediate phase to α-$FAPbI_3$ with coarsening of grains. This grain coarsening can be explained by the Turnbull theory. It is worth noting that the grain growth observed cannot be solely attributed to the Ostwald ripening process. Instead, the thermodynamic driving force for grain size is primarily dependent on the dihedral angle (φ), which determines the overall energy required for changes in grain size during the transformation. If the dihedral angle (φ) is greater than 120° (resulting in a convex grain boundary with more than 6 faces), then the size of the grains will increase. On the other hand, if the dihedral angle is less than 120° (creating a concave grain boundary with less than 6 faces), then the size of the grains will decrease, as the system has a tendency to shift towards minimal surface energy. However, at φ = 120° (six faces) all grains are usually stable as shown in Fig. 3c. This grain growth can be represented mathematically as follows:[29]

$$r_t^n - r_o^n = K_s^t$$

where r_0 = grain radius at time zero, r_t = grain radius at time 't', generally n = 2, and K_s is the grain growth rate. Hence, it has been observed (Fig. 3e and f) that all grains having six or more faces started to grow with the increase in annealing time, resulting in their transformation into larger and more compact grains. Meanwhile, grains with less than six faces diffused into larger grains during this process.

Based on XRD and SEM results, it is evident that the proposed novel approach led to the formation of an intermediate phase (FAI-PbI_2-DMSO), which demonstrated stability from room temperature to up to 150 °C. After reaching the substrate temperature at 150 °C, the slow removal of DMSO can be visualized in Fig. S2 (ESI†). Following the completion of the annealing process, the intermediate phase slowly transformed into α-$FAPbI_3$ (as shown in Video S2, ESI†).

(b) Calculation of induced strain on different substrates due to different TECs. Since crystallization starts from the substrate side and propagates upwards, there is strong contact between the top of the substrate and the bottom of the growing crystal interface. Consequently, while undergoing the annealing process to facilitate the intermediate phase to α-$FAPbI_3$ phase transition, there is molar volume contraction, resulting in a strained film being formed on the substrate. The molar volume contraction in the film primarily occurs due to lattice mismatch

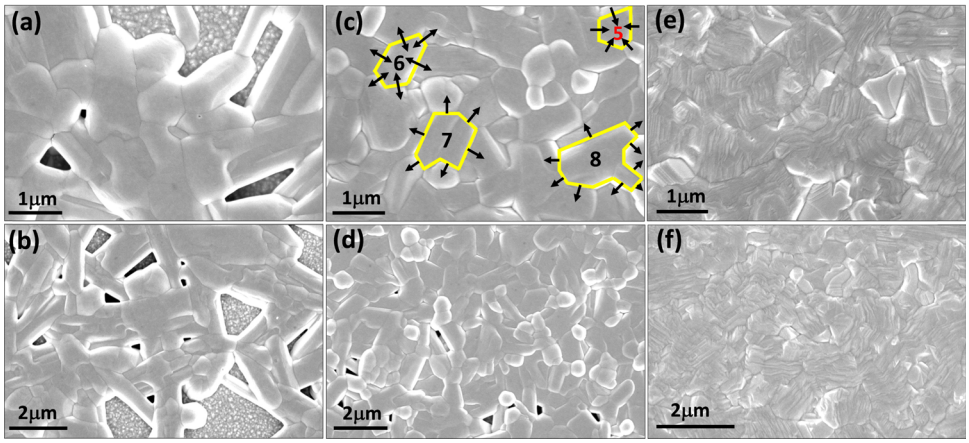

Fig. 3 SEM images (top-view) of (a) and (b) the FAI-PbI_2-DMSO intermediate phase at different magnifications, (c) and (d) perovskite phase transformation from the FAI-PbI_2-DMSO intermediate phase to $FAPbI_3$ with convex curvature grain growth ($\varphi > 120°$) at 150 °C at different magnifications, and (e) and (f) α-$FAPbI_3$ at different magnifications.

and different thermal expansion coefficients between the perovskite and the substrate. Collectively, these elements generate adequate strain within the film, thereby achieving the stabilization of the α-$FAPbI_3$ phase at room temperature (R.T.).[30] Hence, for the estimation of strain present in the α-$FAPbI_3$ film on two different substrates S1 (glass/FTO/SnO_2) and S2 (glass substrate), the films were analysed by theoretical calculations and microstructural stress analysis using XRD. Therefore, the strain values in the perovskite film were theoretically estimated using the following equation:[31]

$$\sigma_{\Delta T} = \frac{E_P}{1-\upsilon_P}(\alpha_s - \alpha_P)\Delta T$$

where Young's modulus E_P = 11.1 GPa[32] and Poisson's ratio (υ_p) = 0.3 of α-$FAPbI_3$.[33] The disparity in thermal expansion coefficients (TEC) at the interfaces of SnO_2/perovskite and glass/perovskite is indicated by $\alpha_s - \alpha_P = 10^{-4}$ K^{-1} and $\alpha_g - \alpha_P = 10^{-5}$ K^{-1} respectively.[34] ΔT is the temperature difference between the substrate (SnO_2 or glass) and the perovskite. Finally, from the above equation the stress value for sample S1 was calculated as 63.43 MPa, whereas for sample S2 it was estimated as 6.3 MPa at ΔT = (343–303) K = 40 K. Additionally, Table S3 (ESI†) displays the theoretical stress calculations at different temperatures.

(c) Microstructural stress analysis for S1 and S2 samples due to lattice mismatch. Microstructural stress analysis was conducted by utilizing XRD to estimate the stress present at a certain fixed depth inside the perovskite film. In this analysis, the software first captures the XRD results at different orientations and based on qualified orientation values it calculates the stress value for a specific 2-theta angle. Here we have calculated the stress for 2-theta = 14° (signature peak for α-$FAPbI_3$) by putting the other corresponding information from Table S4 (ESI†) in the software for the analysis of samples S1 and S2. The analysis of stress for sample S1 is showing a relatively high tensile stress (strain) value of 140.8 MPa, mainly due to comparatively higher Gibbs free energy caused by unit cell expansion. This expansion is mainly caused by lattice mismatch between SnO_2 (lattice parameters: $a = b = 0.47$ nm, $c = 0.31$ nm)[35] and α-$FAPbI_3$ (lattice parameters: $a = b = c = 0.64$ nm)[36] along with different thermal expansion coefficients of SnO_2 and the α-$FAPbI_3$ film. On the other hand, sample S2 possesses a lower stress value of 2.96 MPa as shown in Fig. S3 and S4 (ESI†). Table 1 presents the calculations of strain and the overall change in strain values from sample S1 to S2.

The obtained stress values are positive, indicating the presence of tensile stress in both samples. This is further supported by the intensity *vs.* 2-theta XRD curve and PL data discussed in the next section. It is noteworthy that the additional stress value in sample S1 is obtained from the TEC data, because of the amalgamation of lattice mismatch and distinct thermal expansion coefficients between SnO_2 and the perovskite. In conclusion, from Sections 2.1(a), (b), and (c), it can be inferred that the controlled growth (formation of the intermediate phase), strain induced from lattice mismatch at the interface (Fig. S5, ESI†), and different thermal expansion coefficients work together to stabilize the α-$FAPbI_3$ phase. However, it is also evident from Fig. 4 that the intermediate phase and mismatch in thermal expansion coefficients alone are not

Table 1 Calculation of strain and change in the strain value from sample S1 to S2

Calculation for the strained sample	Calculation for the unstrained sample	$\Delta\varepsilon = \left(\frac{\varepsilon_1 - \varepsilon_2}{\varepsilon_1}\right) \times 100$
Young's modulus = 11.1 GPa Stress = 140.87 Mpa ε_1 (strain) $= \left(\frac{140.87}{11\,100}\right) = 0.0127$	Young's modulus = 11.1 GPa Stress = 2.96 MPa ε_2 (strain) $= \left(\frac{2.96}{11\,100}\right) = 0.00027$	97.87%

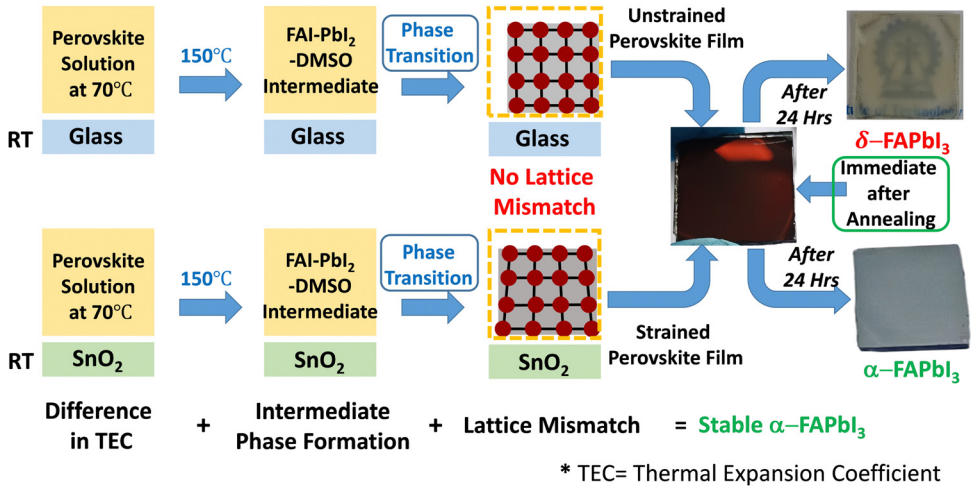

Fig. 4 Stabilization route for the α-$FAPbI_3$ phase and film stability after 24 hours on SnO_2 (strained substrate) and glass (unstrained substrate).

enough to stabilize the α-$FAPbI_3$ phase. To augment the comprehensiveness of phase stabilization across a range of substrates, the visualization of this phenomenon is presented in Fig. S8 (ESI†).

(d) Characteristics of the strained film (samples S1 and S2). Both samples (S1 and S2) were further characterized through XRD and photoluminescence spectroscopy (PL) to validate the strain present in the α-$FAPbI_3$ film. The XRD data show a peak shifting towards a lower 2-theta value indicating the presence of tensile stress in the sample.[37] Fig. 5a shows the XRD data of the characteristic peak for the α-$FAPbI_3$ phase of both samples. The XRD data from sample S1 display an evident shift towards a reduced 2-theta angle, signifying the existence of elevated tensile stress within the perovskite film arising from lattice mismatch and varying thermal expansion coefficients. On the other hand, the XRD pattern of sample S2 shows a relatively small shift towards a lower 2-theta angle, indicating the presence of lower tensile stress in the perovskite film. The interplanar distance (d) of certain crystal planes can be calculated from the XRD pattern using the Bragg's law, which is given by

$$n\lambda = 2d\sin\theta$$

where n is showing the order of reflection (an integer value), λ is the wavelength of X-rays, θ is the Bragg's angle, and d is the interplanar distance. By measuring the Bragg's angle (θ) and using the known value of λ, the interplanar distance can be calculated. The interplanar distance 'd' was utilized to compute the percentage change in strain between the samples, employing the following equation:

$$\varepsilon = \frac{d_{S1(hkl)} - d_{S2(hkl)}}{d_{S2(hkl)}}$$

The d-spacing of samples S1 and S2 was analysed as $d_{S2}(hkl)$ = 6.31764 Å and $d_{S2}(hkl)$ = 6.35943 Å respectively. This resulted in an overall change in the interplanar spacing of Δd (%) = 0.66%. Based on these calculations, it is evident that there is a clear change in the interplanar distance of both samples, which provides sufficient proof for the presence of strain in the α-$FAPbI_3$ film. Furthermore, a study by Dongtao Liu *et al.* reported a shift in the PL peak of the α-$FAPbI_3$ phase towards

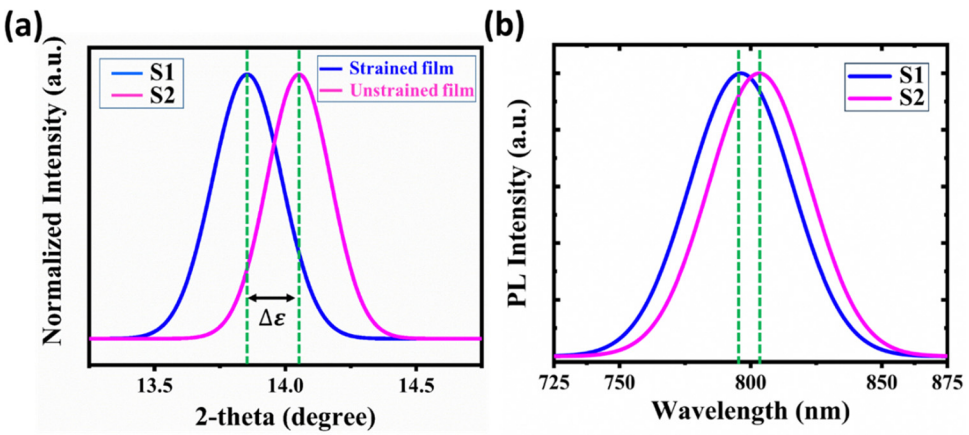

Fig. 5 (a) XRD analysis: shifting of the peak and strain difference in strained (S1) and unstrained (S2) samples, and (b) PL spectra of the $FAPbI_3$ film: with increased strain, peak shifting of the α-$FAPbI_3$ phase towards the higher bandgap side.

a lower wavelength due to lattice expansion.[38] In the PL plot of the current study, the peak of the S1 sample is observed to shift towards the lower wavelength, indicating an increase in the bandgap of the strained S1 sample due to lattice expansion, as shown in Fig. 5b.

Therefore, the XRD and PL results support the presence of stress in both samples, S1 and S2, which is governed by microstructural stress analysis for lattice mismatch, as well as theoretical estimation of stress due to mismatch in thermal expansion coefficients.

2.2. Phase characterization

The fabricated perovskite film on the SnO_2 substrate was subjected to characterization to identify the formation of the α-$FAPbI_3$ phase. Fig. 6c shows the XRD pattern of α-$FAPbI_3$, which confirms the formation of α-$FAPbI_3$ with a strong characteristic peak of 2-theta at ≈14°, as reported earlier.[26] The fabricated perovskite film on the SnO_2 substrate was characterized to indicate the formation of the α-$FAPbI_3$ phase. The absence of a peak at 2-theta ≈12.7°, which is the characteristic peak of PbI_2, indicates the complete conversion of α-$FAPbI_3$ or the absence of residual PbI_2 after the transformation of the perovskite phase from the intermediate phase. In addition, optical characterization of α-$FAPbI_3$ was performed through UV-absorbance and PL spectroscopy analysis. The UV-Vis absorbance plot is shown in the inset of Fig. 6a. It can be seen that the absorption onset is approximately at 820 nm. The corresponding Tauc plot is shown in Fig. 6a which indicates that the bandgap of the material is 1.51 eV. Similarly, the PL peak was recorded at 804 nm which is corresponding to 1.54 eV. Both these results provide support for the bandgap corresponding to the α-$FAPbI_3$ film, as reported earlier.[39] The presence of nitrogen (N), lead (Pb), carbon (C), and iodine (I) elements in the perovskite film was further investigated by utilizing XPS analysis. In this analysis, the XPS survey and specific elemental analysis provide the binding energy of N 1s, C 1s, I 3d, and Pb 4f. The C 1s and N 1s XPS spectra of α-$FAPbI_3$ showed a specific peak at 287 eV and 400.01 eV, respectively, which is the signature peak for FA. The doublet of Pb $4f_{7/2}$ and $4f_{5/2}$ appeared at 137 eV and 141.84 eV, while for I $3d_{5/2}$ and I $3d_{3/2}$ it was recorded at 617.8 eV and 629.3 eV respectively. The peak doublet difference of Pb and I was found at 4.84 eV and 11.5 eV, as shown in Fig. S6 (ESI†). All these values are similar to the reported corresponding values of α-$FAPbI_3$, which supports the formation of the α-$FAPbI_3$ phase.[40]

Finally, elemental mapping was also performed for the identification of approximate percentage of elements present in the perovskite film. The elemental analysis showed only the presence of C, N, Pb, and I elements, with the percentage value corresponding to α-$FAPbI_3$ shown in Fig. S7 (ESI†), which further supported the formation of $FAPbI_3$. Hence, the formation of α-$FAPbI_3$ on the SnO_2 substrate is confirmed by UV-Vis, PL, XRD, XPS, and EDS characterization.

2.3. Phase stability of the perovskite film

The degradation of a hybrid perovskite film typically initiates from grain boundaries and pinholes due to their high surface energy. The formamidinium cation (FA^+) present in the film can easily break down under prolonged exposure to humidity, leaving behind unbonded Pb^{2+} and I^- ions in the α-$FAPbI_3$ film. This process further accelerates the deterioration (degradation) of the perovskite film. The degradation process can be described by the following expression:[41]

$H_2N–CH–NH_2PbI_3 \rightarrow H_2N–CH–NH_2I + PbI_2$ (Solid)

In this study, we initially considered four samples (fresh S1, S1.1 aged for one month, S1.2 aged for two months, and S1.3 aged for three months) on SnO_2-coated substrates to investigate the phase stability at regular time intervals under ambient conditions (relative humidity >40%, under indoor light) using XRD. Fig. 7 illustrates that for sample S1, there is complete formation of α-$FAPbI_3$, as discussed in Section 2.2. The XRD pattern for sample S1.1 indicates that the alpha-phase of α-$FAPbI_3$ begins to deteriorate, as evidenced by the appearance of a signature peak of PbI_2 at 2-theta ≈12.7°. The intensity of the PbI_2 peak increases with time for samples S1.2 and S1.3; however, there is no evidence of δ-$FAPbI_3$ in the XRD data. Thus, the black α-$FAPbI_3$ phase formed on the SnO_2 substrate degrades over time under ambient conditions (relative humidity >40%, under indoor light) without transformation into δ-$FAPbI_3$.

The phase stability of α-$FAPbI_3$ was further examined by using XPS and SEM for two extreme samples, *i.e.,* S1 and S1.3, under ambient conditions (RH > 40%, under indoor light). XPS analysis can provide information regarding the stability of α-$FAPbI_3$ by examining the change in the binding energy of Pb^0, Pb^{2+}, I^- ions, *etc.,* over time under humid conditions. Fig. S10 (ESI†) illustrates the XPS survey spectra for both samples. The observed shift in the XPS peak intensity towards higher binding

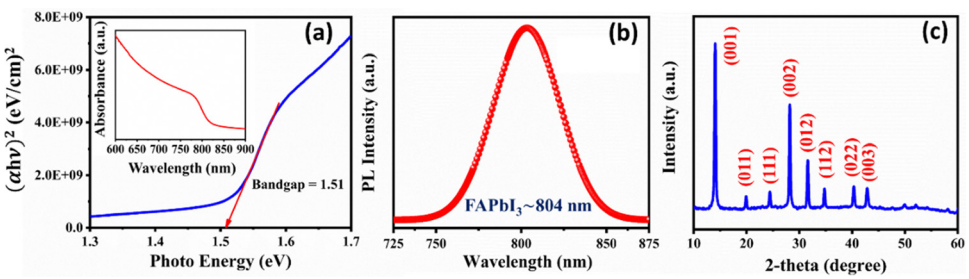

Fig. 6 Characterization of the $FAPbI_3$ film: (a) Tauc and absorbance plot, (b) PL spectra, and (c) XRD pattern.

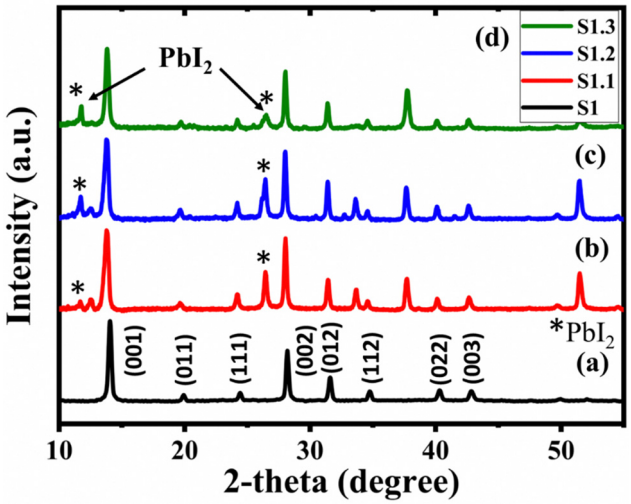

Fig. 7 XRD pattern of the α-$FAPbI_3$ film on glass/FTO/SnO_2 coated substrates: (a) sample S1 at 0 hours, (b) sample S1.1 after 1 month, (c) sample S1.2 after 2 months, and (d) sample S1.3 after 3 months.

energy indicates a change in the nature of chemical bonding or a change in the oxidation state. The Pb 4f core electron peak for sample S1.3 has shifted towards the higher binding energy side, with an increase in the peak area compared to sample S1 (Fig. S9a, ESI†). The observed peak shift and broadening are consistent with the formation of PbI_2 or uncoordinated Pb^{2+} ions in sample S1.3. Similarly, the I 3d peak for sample S1.3 has also shifted towards the high binding energy side, with a decrease in the peak area, likely due to the degradation of α-$FAPbI_3$ (Fig. S9b, ESI†). Therefore, the XPS results provide a rough estimate of the degradation of the alpha-phase of $FAPbI_3$ under relative humidity greater than 40%. The XRD analysis of S1 and S1.3 samples also demonstrates the phase stability of the α-$FAPbI_3$ film. For sample S1.3, the alpha-phase degraded into a mixture of alpha-phase and lead iodide phase after three months, with no evidence of delta-phase formation, as shown in Fig. S11 (ESI†). Similarly, the deformation of the alpha-phase of α-$FAPbI_3$ can be visualized through the top view of SEM images of both samples. In sample S1.3, it can be clearly seen that humidity degraded the alpha-phase of $FAPbI_3$. However, for sample S1, both XRD and top view of SEM results demonstrate the stability of the pure alpha-phase of $FAPbI_3$ with compact grains.

2.4. Device characterization

The performance assessment of the device was conducted using a *J–V* measurement unit. The structure of the device and its energy band diagram for the current investigation is depicted in Fig. S1 (ESI†). The results displayed in Fig. 8a demonstrate that the most efficient cell achieved a PCE of

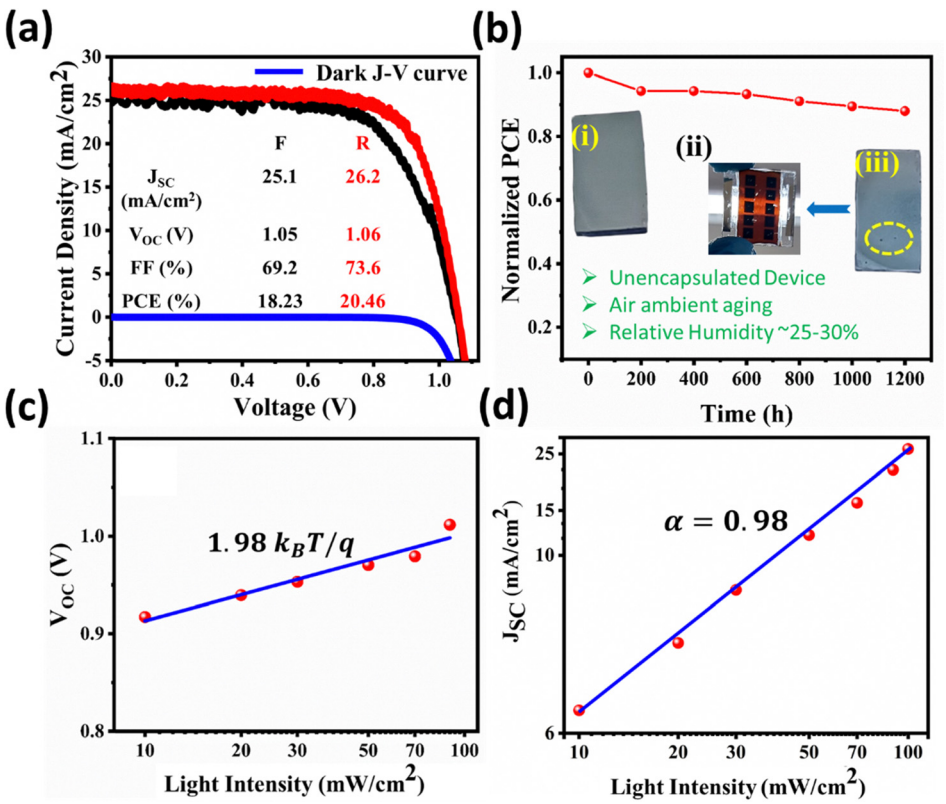

Fig. 8 (a) *J–V* curve in the forward and reverse direction (best performing device), (b) normalized performance (stability) of the unencapsulated device when exposed to 25–30% RH in an air ambient environment for different time periods, and (i), (ii), and (iii) represent the ambient stored film under RH 25–30%, ambient stored device under RH 25–30%, and ambient stored film under RH 60–70% (showing degradation) respectively. Light intensity dependent study of $FAPbI_3$ based PSCs: (c) light intensity *versus* V_{OC} and (d) light intensity *versus* J_{SC} on a logarithmic scale.

20.46% during the reverse scan. This was accompanied by a current density (J_{SC}) of 26.2 mA cm^{-2}, an open circuit voltage (V_{OC}) of 1.06 V, and a fill factor (FF) of 73.6%. Moreover, the average device characteristics of 25 cells are shown in Table S5 (ESI†). Notably, the normalized PCE of the device without encapsulation in an air-ambient environment remained above 85% even after a prolonged ambient exposure of 1200 hours (Fig. 8b). The *J–V* measurements were executed under the standard testing conditions of AM1.5G illumination, with an intensity of 100 mW cm^{-2}.

Under operational conditions, the V_{OC} and J_{SC} of solar cells are dependent on incident light intensity, which provides the information of ideality factor '*n*' and formation of the space charge limited region (α value). Therefore, the fabricated device was investigated under various light intensities from 100 mW cm^{-2} to 10 mW cm^{-2} using neutral density (ND) filters. The light intensity *versus* V_{OC} plot provides information about the ideality factor '*n*' (shows the trap-assisted recombination in solar cells) by using the following mathematical expression:[18]

$$V_{OC} \propto \frac{nk_B T}{q} \log_{10} I_0$$

where n, k_B, T, I, and q respectively stand for the ideality factor, Boltzmann's constant, absolute temperature, light intensity, and elementary charge.

The ideality factor was calculated to be n = 1.98, as demonstrated in Fig. 8c. This value is close to 2, indicating the presence of recombination losses caused by defects, such as interfacial or bulk defects, or both. Additionally, the power law dependence of light intensity and J_{SC} ($J \propto I^{\alpha}$) was observed under operational conditions. The value of 'α' was calculated by plotting the graph between light intensity and J_{SC} on a logarithmic scale, as illustrated in Fig. 8d. The 'α' value determines the formation of the space charge limited region. In the current study, the investigated device showed $\alpha \sim 0.98$, which is very close to 1, implying mostly excited carriers are separated prior to recombination. Thus, these findings demonstrate that the device exhibits reasonable efficiency and performance stability, with the formation of a limited space charge region under operational conditions. Nevertheless, the poor ideality factor suggests the presence of a significant number of interfacial or bulk defects. The performance of our fabricated solar cell is analyzed in comparison to previously reported data. Our analysis showed a significant improvement in stability when contrasted with other reported performances (Table 2).

3. Conclusion

In summary, a successful stabilization approach for the photoactive α-$FAPbI_3$ phase without the use of additives was demonstrated. In order to achieve the stabilization of the photoactive α-$FAPbI_3$ phase, a strategic spin coating process was employed. This process facilitated the formation of an intermediate phase, driven by the strain generated due to the variations in the thermal expansion coefficient (α) between the perovskite precursor solution and the substrate. Additionally, this phenomenon was influenced by the lattice mismatch existing between SnO_2 and the α-$FAPbI_3$ phase. The intermediate was characterized using XRD and SEM. The formed α-$FAPbI_3$ on the SnO_2 substrate was confirmed using PL, XRD, XPS, UV-Vis, and EDS characterization. The stability of the α-$FAPbI_3$ film on SnO_2 coated substrates was analysed over time, based on the XRD pattern and SEM images. The observation showed the dissociation of the α-$FAPbI_3$ phase into PbI_2 after a substantial time in an air ambient environment. However, there was no evidence for the transformation of the δ-$FAPbI_3$ phase in the film. The assessment of device efficiency and stability was conducted through *J–V* measurements. The most exceptional cell demonstrated a PCE of 20.46%, accompanied by an ideality factor of 1.98 and an α value of 0.98. It is noteworthy that the non-encapsulated device retained normalized PCE above 85% when stored under relative humidity levels below 40% even after enduring 1200 hours. Overall, the proposed approach provides a pathway for the fabrication of additive-free α-$FAPbI_3$ based PSCs for efficient and long-term stability on SnO_2 coated substrates.

4. Experimental section

Materials

15% Tin(IV) oxide in H_2O colloidal dispersion was purchased from Alfa Aesar. Formamidinium iodide (FAI; 99.99%), lead(II)

Table 2 Performance stability of non-encapsulated $FAPbI_3$-based perovskite solar cells under RH below 30%

Device structure	Additive	Aging time (hours)	Retained normalized PCE	Ref.
FTO/SnO_2/$FAPbI_3$/Spiro-OMeTAD/Au	$Pb(Ac)_2$	800	~0.9	42
FTO/TiO_2/$(TMS)_{0.02}(FA)_{0.98}PbI_3$/Spiro-OMeTAD/Au	Trimethylsulfonium cation (TMS^+) doping	100	~0.8	43
FTO/SnO_2/$FAPbI_3$/Spiro-OMeTAD/Au	$[Pb_3I_6(Ac)_4]^{4-}$	1000	~0.85	44
FTO/SnO_2/$FAPbI_3$/Spiro-OMeTAD/MoO_3/Ag	Naphthylmethylammonium iodide	432	<0.73	45
FTO/TiO_2/$FAPbI_3$/Spiro-OMeTAD/Au	*N*-Butyl-*N*-methyl-piperidinium bromide $[BMP]^+[Br]^-$	960	<0.9	46
ITO/PTAA/$FAPbI_3$/PCBM/BCP/Ag	Phenylethylammonium iodide (PEAI)	648	~0.97	47
ITO/PEDOT:PSS/$FAPbI_3$/Spiro-OMeTAD/Ag	2-Thiophenemethylammonium (TMA)	1200	~0.8	48
ITO/MeO-2PACz/$FAPbI_3$/PCBM/BCP/Ag	MeO-2PACz	800	<0.9	49
ITO/SnO_2/$FAPbI_3$/Spiro-OMeTAD/Au	4-Fluorobenzamide	1000	~0.9	50
FTO/PTAA/Al_2O_3 nanoparticles/perovskite/LiBr/C70/Zr $(ac\text{-}ac)_4$/Au	Dimethylammonium cation	1130	~0.8	51
FTO/SnO_2/$FAPbI_3$/Spiro-OMeTAD/MoO_3/Au	Ammonium acetate	1000	~0.95	52
FTO/SnO_2/$FAPbI_3$/Spiro-OMeTAD/Ag	Without additive	1200	~0.85	Our work

iodide (PbI_2; 99.98%), and 4-*tert*-butylpyridine (*t*-BP) were purchased from Tokyo Chemical Industry (TCI). Dimethyl sulfoxide (DMSO; >99%), *N*′*N*′-dimethylformamide (DMF; >99%), 2-propanol (IPA; >98%), toluene (>98%), chlorobenzene (>98%), acetonitrile (ACN) (>99%) and acetone (>98%) solvents were purchased from Merck. Hellmanex soap solution, bis(trifluoromethane) sulfonimide lithium salt (Li-TFSI; 99.95%), and Spiro-OMeTAD were purchased from Sigma-Aldrich. The 2.2 mm thick FTO-coated glasses with sheet resistance 15 Ω $\square^{-1}$ were purchased from Greatcell Solar Materials.

The mentioned materials were used as received.

Device fabrication

All the devices and films for the characterization were fabricated under air ambient conditions with controlled humidity (<40% RH). FTO glass substrates (TEC-15, 15 Ω $\square^{-1}$) of 2.5 × 2.5 cm^2 area were cleaned thoroughly with detergent (2% Hellmanex in DI water), DI water, acetone, and propanol-2 by ultrasonication. The nitrogen dried FTO substrates were further treated with UV-Ozone for 20 minutes. A thin layer of SnO_2 film was spin coated on the cleaned FTO substrates. For the deposition, the 15% tin(IV) oxide in H_2O colloidal solution was diluted 1 : 6 V/V in DI water. The prepared solution was sonicated for 30 minutes followed by stirring for 10 minutes at 600 rpm. Then 150 μL solution was used for the deposition of each SnO_2 layer with spinning at 3000 rpm (rotation per minute) for 30 seconds. Then, SnO_2 spin coated substrates were dried at 120 °C for 60 minutes. The precursor solution of the perovskite was prepared by mixing 0.7 M FAI and 0.7 M PbI_2 in DMF and DMSO solvent at 3 : 1 and heating the mixed solution at 75 °C with stirring at 800 rpm for 60 minutes.

The prepared solution was spin coated onto SnO_2 coated substrates in three steps, with the first step at 500 rpm for 5 sec, the second step at 3500 rpm for 5 seconds, and the third step at 5000 rpm for 30 sec. In the third step at the 15th second, 250 μL of toluene as anti-solvent was dripped. The deposited perovskite film was annealed at 150 °C for 30 minutes (as shown in Video S1, ESI†). The solution of Spiro-OMeTAD was prepared by taking 60 mg of Spiro-OMeTAD in 640 ml of chlorobenzene along with 24 μL of 0.6 M Li-TFSI in acetonitrile and 11.5 μL of *t*-BP. The prepared solution was heated at 65 °C with string at 600 rpm for 30 minutes. An 80 μL Spiro-OMeTAD solution was used for each deposition on the perovskite film with the spin coating speed of 2000 rpm for 30 seconds. In the final step, an 80 nm thick silver layer was deposited using a thermal evaporation unit onto the top of the HTL (spiro) layer, while maintaining a cell area of 0.09 cm^2.

Material and device characterization

XRD analysis and microstructural stress analysis were performed by utilizing the Bruker D8 Discover diffractometer system. Morphological characterization was done by using a Zeiss MERLIN scanning electron microscope (SEM). Photoluminescence analysis was conducted using a Horiba iHR 320 spectrometer. XPS investigations were performed utilizing a PHI 5000 VERSA PROBE III model. UV-visible absorption spectroscopy was carried out employing an Avantes Starline AvaSpec-ULS364 UV-visible spectrometer. The solar simulator used for generating an AM 1.5G simulated spectrum at an intensity of 100 W cm^{-2} was a Peccell Technologies PEC-L01 model, with ND filters enabling intensity adjustments. *J*–*V* measurements were executed using a Keithley 2450 SMU. The stability assessments of the devices were conducted in an unencapsulated state under dark ambient conditions.

Conflicts of interest

The authors declare no conflict of interest.

Acknowledgements

S. P. and N. K. B. express gratitude to the Prime Minister's Research Fellows (PMRF) scheme for the research fellowship. T. S. appreciates the Science and Engineering Research Board (SERB) for funding (IPA/2021/000081). Additionally, T. S. acknowledges the infrastructure and research facilities provided by IIT Kharagpur and IIT Delhi.

References

1 V. D'Innocenzo, A. R. Srimath Kandada, M. De Bastiani, M. Gandini and A. Petrozza, *J. Am. Chem. Soc.*, 2014, **136**, 17730–17733.
2 Y. Ogomi, A. Morita, S. Tsukamoto, T. Saitho, N. Fujikawa, Q. Shen, T. Toyoda, K. Yoshino, S. S. Pandey, T. Ma and S. Hayase, *J. Phys. Chem. Lett.*, 2014, **5**, 1004–1011.
3 H. J. Snaith, *J. Phys. Chem. Lett.*, 2013, **4**, 3623–3630.
4 S. D. Stranks, G. E. Eperon, G. Grancini, C. Menelaou, M. J. P. Alcocer, T. Leijtens, L. M. Herz, A. Petrozza and H. J. Snaith, *Science*, 2013, **342**, 341–344.
5 Y. Zhang, A. Kirs, F. Ambroz, C.-T. Lin, A. S. R. Bati, I. P. Parkin, J. G. Shapter, M. Batmunkh and T. J. Macdonald, *Small Methods*, 2021, **5**, 2000744.
6 A. S. R. Bati, L. Yu, S. A. Tawfik, M. J. S. Spencer, P. E. Shaw, M. Batmunkh and J. G. Shapter, *iScience*, 2019, **14**, 100–112.
7 T. Singh and T. Miyasaka, *Adv. Energy Mater.*, 2018, **8**, 1700677.
8 T. Singh, S. Öz, A. Sasinska, R. Frohnhoven, S. Mathur and T. Miyasaka, *Adv. Funct. Mater.*, 2018, **28**, 1706287.
9 S. Ghosh, B. Boro, S. Porwal, S. Mishra and T. Singh, *Energy Adv.*, 2023, **2**, 1155–1165.
10 S. Ghosh, S. Mishra and T. Singh, *Adv. Mater. Interfaces*, 2020, **7**, 2000950.
11 N. K. Bansal, S. Ghosh, S. Porwal and T. Singh, *J. Mater. Sci.: Mater. Electron.*, 2023, **35**, 1.
12 J. Park, J. Kim, H.-S. Yun, M. J. Paik, E. Noh, H. J. Mun, M. G. Kim, T. J. Shin and S. I. Seok, *Nature*, 2023, **616**, 724–730.
13 L. M. Pazos-Outón, T. P. Xiao and E. Yablonovitch, *J. Phys. Chem. Lett.*, 2018, **9**, 1703–1711.

14 M. B. Johnston and L. M. Herz, *Acc. Chem. Res.*, 2016, **49**, 146–154.
15 Z. Song, A. Abate, S. C. Watthage, G. K. Liyanage, A. B. Phillips, U. Steiner, M. Graetzel and M. J. Heben, *Adv. Energy Mater.*, 2016, **6**, 1600846.
16 Y. H. Park, I. Jeong, S. Bae, H. J. Son, P. Lee, J. Lee, C.-H. Lee and M. J. Ko, *Adv. Funct. Mater.*, 2017, **27**, 1605988.
17 S. Masi, A. F. Gualdrón-Reyes and I. Mora-Seró, *ACS Energy Lett.*, 2020, **5**, 1974–1985.
18 S. R. Cowan, A. Roy and A. J. Heeger, *Phys. Rev. B: Condens. Matter Mater. Phys.*, 2010, **82**, 245207.
19 S.-H. Turren-Cruz, A. Hagfeldt and M. Saliba, *Science*, 2018, **362**, 449–453.
20 S. D. Stranks and H. J. Snaith, *Nat. Nanotechnol.*, 2015, **10**, 391–402.
21 N. K. Bansal, S. Porwal and T. Singh, *Surf. Interfaces*, 2024, **44**, 103738.
22 F. Brivio, C. Caetano and A. Walsh, *J. Phys. Chem. Lett.*, 2016, **7**, 1083–1087.
23 M. C. Brennan, S. Draguta, P. V. Kamat and M. Kuno, *ACS Energy Lett.*, 2018, **3**, 204–213.
24 N. J. Jeon, J. H. Noh, Y. C. Kim, W. S. Yang, S. Ryu and S. I. Seok, *Nat. Mater.*, 2014, **13**, 897–903.
25 Y. Tu, J. Wu, X. He, P. Guo, H. Luo, Q. Liu, J. Lin, M. Huang, Y. Huang, L. Fan and Z. Lan, *Appl. Surf. Sci.*, 2017, **403**, 572–577.
26 S. Wang, Y. Chen, R. Li, Y. Xu, J. Feng, D. Yang, N. Yuan, W.-H. Zhang, S. Liu and J. Ding, *Adv. Sci.*, 2020, **7**, 1903009.
27 Y. Bai, S. Xiao, C. Hu, T. Zhang, X. Meng, Q. Li, Y. Yang, K. S. Wong, H. Chen and S. Yang, *Nano Energy*, 2017, **34**, 58–68.
28 N. Ahn, D.-Y. Son, I.-H. Jang, S. M. Kang, M. Choi and N.-G. Park, *J. Am. Chem. Soc.*, 2015, **137**, 8696–8699.
29 W. D. Kingery, H. K. Bowen and D. R. Uhlmann, *Introduction to ceramics*, John wiley & sons, 1976.
30 S.-Y. Ju, W. I. Lee and H.-S. Kim, *ACS Appl. Mater. Interfaces*, 2022, **14**, 39996–40004.
31 N. Rolston, K. A. Bush, A. D. Printz, A. Gold-Parker, Y. Ding, M. F. Toney, M. D. McGehee and R. H. Dauskardt, *Adv. Energy Mater.*, 2018, **8**, 1802139.
32 S. Sun, F. H. Isikgor, Z. Deng, F. Wei, G. Kieslich, P. D. Bristowe, J. Ouyang and A. K. Cheetham, *ChemSusChem*, 2017, **10**, 3740–3745.
33 Y. Chen, Y. Lei, Y. Li, Y. Yu, J. Cai, M.-H. Chiu, R. Rao, Y. Gu, C. Wang, W. Choi, H. Hu, C. Wang, Y. Li, J. Song, J. Zhang, B. Qi, M. Lin, Z. Zhang, A. E. Islam, B. Maruyama, S. Dayeh, L.-J. Li, K. Yang, Y.-H. Lo and S. Xu, *Nature*, 2020, **577**, 209–215.
34 D.-J. Xue, Y. Hou, S.-C. Liu, M. Wei, B. Chen, Z. Huang, Z. Li, B. Sun, A. H. Proppe, Y. Dong, M. I. Saidaminov, S. O. Kelley, J.-S. Hu and E. H. Sargent, *Nat. Commun.*, 2020, **11**, 1514.
35 M. Zheng, J. Ni, F. Liang, M.-C. Wang and X. Zhao, *J. Alloys Compd.*, 2016, **663**, 371–378.
36 M. T. Weller, O. J. Weber, J. M. Frost and A. Walsh, *J. Phys. Chem. Lett.*, 2015, **6**, 3209–3212.
37 C. Zhu, X. Niu, Y. Fu, N. Li, C. Hu, Y. Chen, X. He, G. Na, P. Liu, H. Zai, Y. Ge, Y. Lu, X. Ke, Y. Bai, S. Yang, P. Chen, Y. Li, M. Sui, L. Zhang, H. Zhou and Q. Chen, *Nat. Commun.*, 2019, **10**, 815.
38 D. Liu, D. Luo, A. N. Iqbal, K. W. P. Orr, T. A. S. Doherty, Z.-H. Lu, S. D. Stranks and W. Zhang, *Nat. Mater.*, 2021, **20**, 1337–1346.
39 Q. Wei, W. Zi, Z. Yang and D. Yang, *Sol. Energy*, 2018, **174**, 933–939.
40 Q. Zhou, L. Liang, J. Hu, B. Cao, L. Yang, T. Wu, X. Li, B. Zhang and P. Gao, *Adv. Energy Mater.*, 2019, **9**, 1802595.
41 S. Tan, I. Yavuz, M. H. Weber, T. Huang, C.-H. Chen, R. Wang, H.-C. Wang, J. H. Ko, S. Nuryyeva, J. Xue, Y. Zhao, K.-H. Wei, J.-W. Lee and Y. Yang, *Joule*, 2020, **4**, 2426–2442.
42 L. Chen, T. Liu, H. Yu, Z. Zhang, C. Qin, N. Zhang, L. Yu, F. Yang, G. Song and Z. Liu, *J. Alloys Compd.*, 2023, **942**, 168924.
43 S. Sandhu, M. M. Rahman, M. Senthilkumar, B. Yadagiri, J. Park, K. Yoo and J.-J. Lee, *J. Power Sources*, 2022, **551**, 232207.
44 X. Jiao, W.-M. Gu, Y. Xu, K.-J. Jiang, G. Yu, Q.-W. Zhang, C.-Y. Gao, C.-M. Liu, X.-H. Fan, L.-M. Yang and Y. Song, *Chem. Eng. J.*, 2023, **452**, 139326.
45 M. Hatamvand, S. Gholipour, M. Chen, Y. Zhou, T. Jiang, Z. Hu, Y. Chen and W. Huang, *Chem. Eng. J.*, 2023, **460**, 141788.
46 C. Duan, Z. Liang, J. Cao, B. Jin, Y. Ming, S. Wang, B. Ma, T. Ye and C. Wu, *ACS Appl. Mater. Interfaces*, 2022, **14**, 43298–43307.
47 K. Wang, J. Huo, L. Cao, P. Yang, P. Müller-Buschbaum, Y. Tong and H. Wang, *ACS Appl. Mater. Interfaces*, 2023, **15**, 13353–13362.
48 J. Liang, A. Sun, Z. Zhang, Y. Zheng, X. Wu, C. Tian, Z. Chen and C.-C. Chen, *ACS Mater. Lett.*, 2023, **5**, 1395–1400.
49 D. Zhang, H. Zhang, H. Guo, F. Ye, S. Liu and Y. Wu, *Adv. Funct. Mater.*, 2022, **32**, 2200174.
50 S. Wang, H. Luo, Z. Gu, R. Zhao, L. Guo, N. Wang, Y. Lou, Q. Xu, S. Peng, Y. Zhang and Y. Song, *Adv. Funct. Mater.*, 2023, **33**, 2214834.
51 D. P. McMeekin, P. Holzhey, S. O. Fürer, S. P. Harvey, L. T. Schelhas, J. M. Ball, S. Mahesh, S. Seo, N. Hawkins, J. Lu, M. B. Johnston, J. J. Berry, U. Bach and H. J. Snaith, *Nat. Mater.*, 2023, **22**, 73–83.
52 D. Wang, M. Chen, X. Zhang, L. Chao, T. Niu, Y. Lv, G. Xing, Y. Xia, M. Li, H. Zhang and Y. Chen, *ACS Appl. Mater. Interfaces*, 2023, **15**, 16818–16827.